

See discussions, stats, and author profiles for this publication at: <https://www.researchgate.net/publication/229737951>

Electrochemical Method for Synthesis of a ZnFe₂O₄/TiO₂ Composite Nanotube Array Modified Electrode with Enhanced Photoelectrochemical Activity

ARTICLE *in* ADVANCED FUNCTIONAL MATERIALS · JULY 2010

Impact Factor: 11.81 · DOI: 10.1002/adfm.200902390

CITATIONS

103

READS

114

5 AUTHORS, INCLUDING:



Qidong Zhao

Dalian University of Technology

118 PUBLICATIONS 2,093 CITATIONS

SEE PROFILE

Electrochemical Method for Synthesis of a $\text{ZnFe}_2\text{O}_4/\text{TiO}_2$ Composite Nanotube Array Modified Electrode with Enhanced Photoelectrochemical Activity

By Yang Hou, Xin-Yong Li,* Qi-Dong Zhao, Xie Quan, and Guo-Hua Chen*

An electrode with intimate and well-aligned $\text{ZnFe}_2\text{O}_4/\text{TiO}_2$ composite nanotube arrays is prepared via electrochemical anodization of pure titanium foil in fluorine-containing ethylene glycol, followed by a novel cathodic electrodeposition method. The deposition of ZnFe_2O_4 is promoted in the self-aligned, vertically oriented TiO_2 nanotube arrays but minimized at the tube entrances. Thus, pore clogging is prevented. Environmental scanning electron microscopy, energy-dispersive X-ray spectra, high-resolution transmission electron microscopy, X-ray diffraction patterns, and X-ray photoelectron spectroscopy indicate that the as-prepared samples are highly ordered and vertically aligned TiO_2 nanotube arrays with ZnFe_2O_4 nanoparticles loading. The TiO_2 nanotubes are anatase with the preferential orientation of $\langle 101 \rangle$ plane. Enhanced absorption in both UV and visible light regions is observed for the composite nanotube arrays. The current–voltage curve of ZnFe_2O_4 -loaded TiO_2 nanotube arrays reveals a rectifying behavior. The enhanced separation of photoinduced electrons and holes is demonstrated by surface photovoltage and photocurrent measurements. Meanwhile, the photoelectrochemical investigations verify that the $\text{ZnFe}_2\text{O}_4/\text{TiO}_2$ composite nanotube array modified electrode has a more effective photoconversion capability than the aligned TiO_2 nanotube arrays alone. In addition, the photoelectrocatalytic ability of the novel electrode is found enhanced in the degradation of 4-chlorophenol.

investigated for photocatalysis,^[1] water splitting for generation of hydrogen,^[2,3] dye-sensitized solar cells,^[4,5] electrochromic windows,^[6] and Li ion batteries.^[7,8] Very recently highly ordered TiO_2 nanotube arrays were synthesized by anodic oxidation of titanium and have generated considerable scientific interest.^[9–11] This simple and more controllable technique was received favorably and further developed by the academic community. In contrast to random nanoparticle systems where slow electron diffusion typically limits device performance,^[12,13] the precisely oriented nature of the crystalline (after annealing) nanotube arrays makes them excellent electron percolation pathways for vectorial charge transfer between interfaces.^[14] Furthermore, the nanotube-array architecture with high surface area ratio and free surface creates an unprecedented opportunity to harvest sunlight for energy conversion or photodegradation more efficiently than the randomly oriented nanoparticles or nanotubes prepared by the sol-gel process.^[15] Because the highly ordered TiO_2 nanotube arrays grows directly on the titanium substrate by anodic oxidation

method, it also has a very strong mechanical strength.^[16]

However, TiO_2 is a large bandgap semiconductor (bandgap of 3.2 eV (anatase)). The intrinsic material absorbs solar light in the UV region only, about 4%–5% of the solar spectrum. From the viewpoint of solar energy utilization, the development of the photocatalysts that can utilize visible light ($\lambda > 400$ nm) efficiently is indispensable. Considerable work by many investigators has focused on improving the absorption of visible light of TiO_2 nanocrystalline by metal^[17–19] and non-metal^[20–22] doping. Although this doping of substitutional atoms improves the visible light absorption in TiO_2 photoelectrode, few of them give prospective satisfactory results because of the increase of carrier-recombination centers, thermal instability,^[23] or the requirement of expensive ion-implantation equipments.^[24] One of the promising strategies to this problem is the development of novel visible-light-active photocatalysts.^[25–29] Another promising solution is the combining TiO_2 with narrow bandgap semiconductors of suitable bandgaps (such as CdS ,^[30–32] PbS ,^[33,34] Bi_2S_3 ,^[35,36] CdSe ,^[37–39] and CdTe ^[40–42]) to extend the absorption

1. Introduction

Nanoscale-architected titania, as a high-efficiency, low-cost photocatalyst, has attracted considerable interest because of its unique chemical and physical properties, and has been widely

[*] Prof. X.-Y. Li, Prof. X. Quan, Dr. Y. Hou, Dr. Q.-D. Zhao
Key Laboratory of Industrial Ecology and Environmental Engineering (MOE)
State Key Laboratory of Fine Chemical
School of Environmental Science and Technology
Dalian University of Technology
Dalian, 116024 (China)
E-mail: xyli@dlut.edu.cn
Prof. X.-Y. Li, Prof. G.-H. Chen
Department of Chemical and Biomolecular Engineering
The Hong Kong University of Science & Technology
Clear Water Bay, Kowloon, Hong Kong (China)
E-mail: kechengh@ust.hk

DOI: 10.1002/adfm.200902390

range of TiO_2 . These semiconductors can serve as sensitizers because they can transfer electrons to the large-bandgap semiconductor under visible light excitation. Meanwhile, heterojunctions might be formed between the different semiconductors, which provide a potential driving force for the separation of photoinduced charge carriers at the interface. This kind of structure will benefit the subsequent charges-participating reactions and improve the energy conversion efficiency of the absorbed photons.

Of particular interest is the development of spinel ZnFe_2O_4 (bandgap 1.86 eV), which is one of the most widely studied materials.^[43–45] It possesses a wide range of functional properties for practical applications, such as magnetic behavior,^[46] electrical characteristics,^[47] absorbent material for hot-gas desulfurization,^[48,49] and so on. Compared to other inorganic semiconducting materials (such as CdS, CdSe, and PbS), ZnFe_2O_4 as a more promising material has received special attention due to its visible light activity, better stability,^[50] and the tunable band edge by modulating grain size, offering an opportunity to harvest most of the visible portion of the solar spectrum.^[51] Recently, Zeng et al.^[52] synthesized the novel $\text{TiO}_2/\text{ZnFe}_2\text{O}_4$ coating by plasma spraying. Yin and co-workers reported that the photoelectrochemical properties of the TiO_2 films can be significantly improved by the introduction of ZnFe_2O_4 nanocrystals.^[53] Xu et al.^[54] prepared zinc ferrite-doped TiO_2 photocatalyst and found good activity in photodegrading methyl orange. However, the energy conversion efficiency is relatively low and it is troublesome to separate and recycle the composite powder from the reaction system. The composite of TiO_2 nanotube arrays with ZnFe_2O_4 may be more promising to overcome the separation problem and improve the energy conversion efficiency because of their superior microstructure as a recyclable electrode.

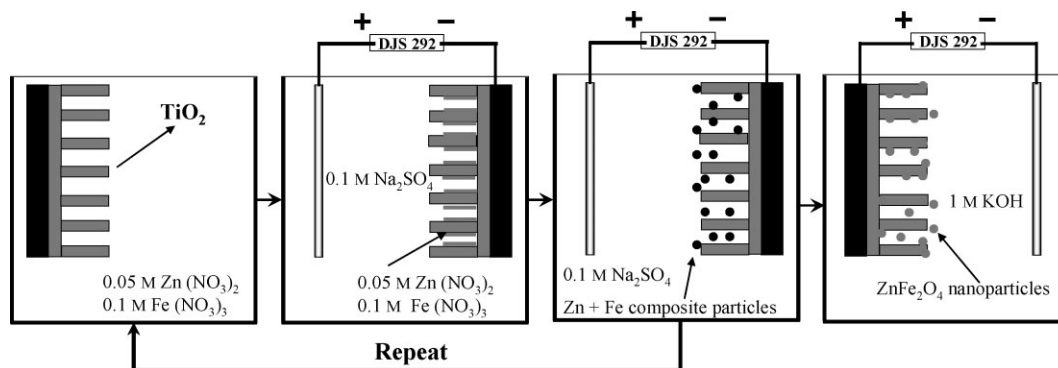
In this paper, highly ordered TiO_2 nanotubular arrays with a wide range of nanotube structure were synthesized by potentiostatic anodization and then loaded with ZnFe_2O_4 nanoparticles via a novel electrodeposition technique. The novel method made the ZnFe_2O_4 nanoparticles deposited in the nanotubes with clogging at the tube entrances minimized. The photoelectrochemical properties were investigated in a standard three-electrode configuration under both UV and visible light irradiation. The promoting effect of the $\text{ZnFe}_2\text{O}_4/\text{TiO}_2$ composite nanotube arrays on the photoelectrocatalytic performance was observed and the correlation between the structure and the property was discussed based on the results of a systematic characterization.

2. Results and Discussion

2.1. Characterization of Photocatalysts

Recently, Mohapatra et al.^[55] reported Fe electrodeposition inside the pore channels of TiO_2 by utilizing the resistance difference between the bottom and top of the nanotubes. The higher resistance on the top of the nanotubes compared to the bottom (which is in contact with the Ti metal) led to successful deposition of Fe into the nanotubes. We have also observed a similar result with as-anodized TiO_2 nanotubes when ZnFe_2O_4 nanoparticles are deposited into the nanotubes while minimizing deposition at the tube entrances. Scheme 1 illustrates the novel deposition procedure. The anodic TiO_2 nanotube arrays are firstly dipped in an electrolyte containing Zn^{2+} and Fe^{3+} , utilizing the capillary action (ultrasonication) to help the salt solution to diffuse through the nanochannels of TiO_2 . Then, metal ions introduced into the nanotubes are electrochemically reduced to form nanoparticles in a new medium that contains only an inert supporting electrolyte without Zn^{2+} and Fe^{3+} by the application of an electric field, which results in deposition of nanoparticles only within the nanotubes. After electrochemically oxidation, the electrodeposited Zn/Fe species are converted into the corresponding oxides as the precursor of ZnFe_2O_4 .

Figure 1 shows the environmental scanning electron microscopy (ESEM), energy-dispersive X-ray spectra (EDX), and high-resolution transmission electron microscopy (HRTEM) images of the TiO_2 nanotube arrays and the $\text{ZnFe}_2\text{O}_4/\text{TiO}_2$ composite nanotube arrays as prepared, respectively. As shown in Figure 1a, TiO_2 nanotube arrays have formed on Ti substrate with the tubes open on the top and close at the bottom. Clearly, these nanotubes are highly ordered, 1D (straight), compactly (nanotubes were well attached to each other) arranged, and vertically aligned (Fig. 1a, inset), with the tubes diameter ranging from 80 to 90 nm and the walls thickness in the range of 15–20 nm. Figure 1b presents the cross-sectional image of the sample anodized at 20 V for 1 h. It is clear that the length of the nanotubes is in the range of 800–1000 nm. TiO_2 nanotube arrays formation in fluoride ion containing electrolytes occurs as a result of the interplay between three simultaneously occurring processes, namely the field-assisted oxidation of Ti metal to form titanium dioxide, the field-assisted dissolution of Ti metal ions in the electrolyte, and the chemical dissolution of Ti and TiO_2 due to etching by fluoride ions. In addition, two key steps in improving the geometry are



Scheme 1. Schematic illustration of a novel developed dipping, deposition, and electrochemically oxidized technique.

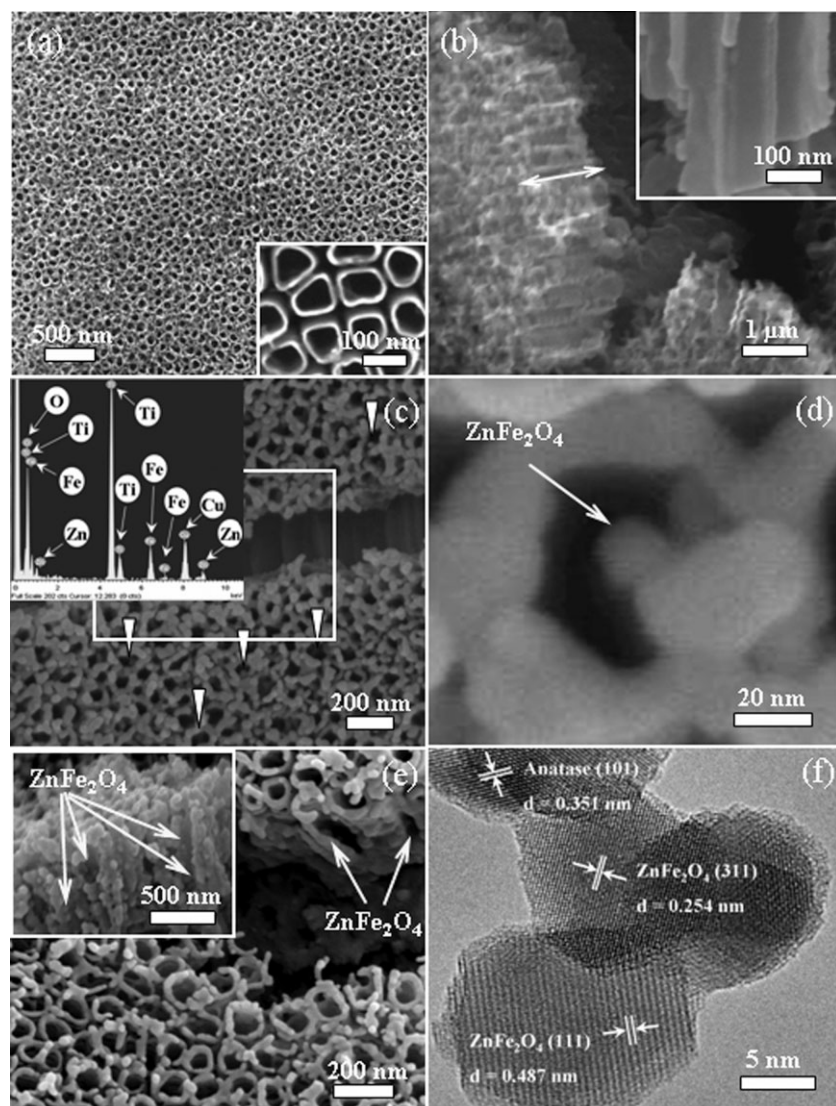


Figure 1. a) Top surface view and b) cross-section view of the TiO_2 nanotube arrays. Insets are the corresponding high-magnification images. c) Top surface view of the $\text{ZnFe}_2\text{O}_4/\text{TiO}_2$ composite nanotube arrays. The inset is the corresponding EDX spectrum. d) High-magnification top surface view of the $\text{ZnFe}_2\text{O}_4/\text{TiO}_2$ composite nanotube arrays. e) Cross-sectional view of the $\text{ZnFe}_2\text{O}_4/\text{TiO}_2$ composite nanotube arrays. Inset is the corresponding high-magnification images. f) HRTEM image of the $\text{ZnFe}_2\text{O}_4/\text{TiO}_2$ composite nanotube arrays.

introduced:^[56,57] i) the use of viscous electrolytes that allowed, under suitable conditions, significantly increase the nanotube growth rate, and ii) the choice of applied anodization voltage that allowed significant improvement on the pore diameter and the tube wall thickness. A detailed discussion of the critical factors for the growth of these structures and controlling the tube/pore geometry has been described previously.^[58–60] Figure 1c and d shows the surface ESEM images of the $\text{ZnFe}_2\text{O}_4/\text{TiO}_2$ composite nanotube arrays. Clearly the uniformly distributed ZnFe_2O_4 nanoparticles with a diameter of approximate 20 nm is successfully promoted in the vertically oriented TiO_2 nanotube arrays but minimized at the tube entrances, indicating that this new method not only effectively suppresses deposition outside of the pores, but

also causes no damage to the ordered structure of the TiO_2 nanotube arrays. The corresponding EDX (Fig. 1c, inset) analysis shows that the loading amounts of ZnFe_2O_4 are about 9.5 at% for the composition. The uniformity of the ZnFe_2O_4 dispersion is obtained via EDX analysis of the $\text{ZnFe}_2\text{O}_4/\text{TiO}_2$ surface at four different places. It is worth pointing out that the high porosity of the TiO_2 nanotube arrays is advantageous for making tiny uniform nanoparticles. The cross-sectional ESEM image double confirms that the excellent uniformity of ZnFe_2O_4 has been deposited successfully into the TiO_2 nanotubes (Fig. 1e). Moreover, nanocrystal structure of $\text{ZnFe}_2\text{O}_4/\text{TiO}_2$ composite nanotube arrays has been investigated by HRTEM measurement along its axial direction (Fig. 1f). The uniform lattice fringe of titania can be observed over an entire primary particle. In addition, the lattice fringes of $d = 0.487$, 0.254 , and 0.351 nm match well with the crystallographic planes of ZnFe_2O_4 $\langle 111 \rangle$, $\langle 311 \rangle$, and anatase TiO_2 $\langle 101 \rangle$, respectively.

To determine the crystal phase of $\text{ZnFe}_2\text{O}_4/\text{TiO}_2$ composite nanotube arrays, the X-ray diffraction (XRD) measurement was carried out with the results shown in Figure 2. All observed peaks can be indexed as peaks generated by ZnFe_2O_4 nanoparticles, TiO_2 nanotube arrays and the Ti substrate, indicating that no Zn or Fe related impurities are present in the ZnFe_2O_4 . The pattern of pure titanium metal is also listed for reference in Figure 2, curve (a). Curve (b) shows a typical XRD pattern of annealed TiO_2 nanotube arrays indicative of a perfect anatase phase. The peak of $\langle 101 \rangle$ crystal face at $2\theta = 25.2^\circ$ indicates a fine preferential growth of the TiO_2 nanotube arrays in the $\langle 101 \rangle$ direction. In addition, the corresponding $\text{ZnFe}_2\text{O}_4/\text{TiO}_2$ composite nanotube arrays synthesized through electrodeposition of the above crystalline TiO_2 , curve (c), exhibited other new characteristic peaks at $2\theta = 30.4^\circ$ of hkl $\langle 220 \rangle$, 35.7° of hkl $\langle 311 \rangle$, and 57.1° of hkl $\langle 511 \rangle$ planes, which are ascribed to the cubic ZnFe_2O_4 with spinel structure (JCPDS file No.79-1150).

The average crystallite size (D) of the ZnFe_2O_4 , 20 nm after calcinations at 773 K, was calculated from the width of the $\langle 311 \rangle$ crystal face using the Scherrer's equation^[61]

$$D = 0.9\lambda / (\beta \cos \theta) \quad (1)$$

where λ is the wavelength of the radiation, β is the corrected peak width at half-maximum intensity (FWHM), and θ is the peak position. Since the line shape was approximately Lorentzian for the samples, the value of β was corrected using the formula $\beta = \beta_m - \beta_{\text{ins}}$, where β_m is the measured peak width and β_{ins} is

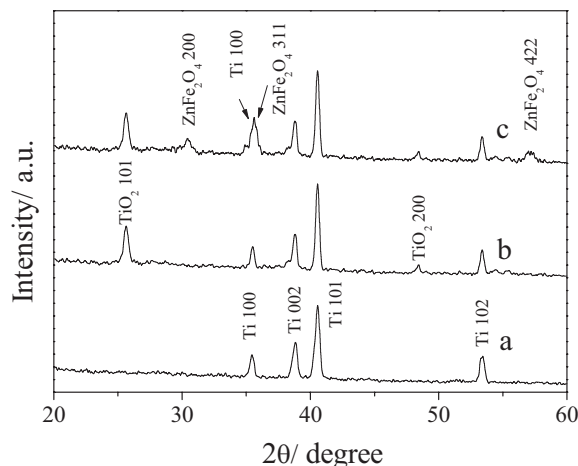


Figure 2. XRD patterns of a) Ti substrate, b) TiO_2 nanotube arrays, and c) $\text{ZnFe}_2\text{O}_4/\text{TiO}_2$ composite nanotube arrays.

the instrumental broadening. Errors in crystallite size were derived by estimating the error in the FWHM to be equal to the 2θ step.^[62]

Figure S1 in the Supporting Information depicts the UV-Vis diffuse reflectance spectra (DRS) of the TiO_2 nanotube arrays and the $\text{ZnFe}_2\text{O}_4/\text{TiO}_2$ composite nanotube arrays. It is clear that TiO_2 absorbs in the UV region with a band edge of 387 nm. However, the spectrum of $\text{ZnFe}_2\text{O}_4/\text{TiO}_2$ composite nanotube arrays absorbs in UV as well as visible region with a band edge of 588 nm (2.11 eV, Fig. S2).

The $\text{ZnFe}_2\text{O}_4/\text{TiO}_2$ composite nanotube arrays were further characterized by fluorescence spectra (FL) (Supporting Information, Fig. S3). The FL intensity of non-loaded nanotubes was much higher than that of ZnFe_2O_4 -loaded nanotubes. The reduction of FL intensity might imply the increased amount of charge separation.^[63] The experimental results demonstrated that the separation ratio of photogenerated electron-hole pairs was quite sensitive to the loading of ZnFe_2O_4 .

X-ray photoelectron spectroscopy (XPS) was employed to reveal the valence states and the surface chemical compositions of the $\text{ZnFe}_2\text{O}_4/\text{TiO}_2$ composite nanotube arrays (Fig. 3). Elements of Ti, Zn, Fe, O, and adventitious C existed in the composite (Fig. 3a). In Figure 3b, two peaks for the Ti 2p were observed at 464.8 and 459.2 eV, assigned to Ti 2p_{1/2} and Ti 2p_{3/2}, respectively. These values agree well with XPS data in the literature and are known to be due to Ti^{4+} in pure anatase titania form.^[64] It seems that the ZnFe_2O_4 loading does not have any significant effect on the position of Ti 2p peak. Among them, The XPS peak for C 1s at 285.38 eV was observed due to adventitious carbon from sample fabrication and/or the XPS instruments

itself (Fig. 3c). As shown in the spectra in Figure 3d, the peaks of 1044.4 and 1022.8 eV can be attributed to Zn 2p_{1/2} and Zn 2p_{3/2}, respectively. This reveals the oxidation state of Zn^{2+} in the composite.^[65] In addition, XPS peaks of Fe 2p located at 710.6 and 724.4 eV should be assigned to the spectra of Fe 2p_{3/2} and Fe 2p_{1/2} for Fe^{3+} (Fig. 3e). The XPS spectra of the O 1s region were also detected, as shown in Figure 3f. The O 1s peak was asymmetric suggesting at least two kinds of oxygen species present in the near-surface region. Meanwhile, the peak for O1s in the composite is broad (Fig. 3f), which can be deconvoluted into three small peaks. The peak located at 532.8 eV is assigned to the adsorbed oxygen.^[66] The peaks located at 529.8 and 531.6 eV are attributed to the O in TiO_2 and ZnFe_2O_4 , respectively.

The surface photovoltage (SPV) method is a well-established non-contact technique for the characterization of semiconductors, which relies on analyzing the illumination-induced changes in the surface voltage.^[67] It can offer important information about semiconductor surface, interface, and bulk properties, including surface band bending, surface and bulk carrier recombination,

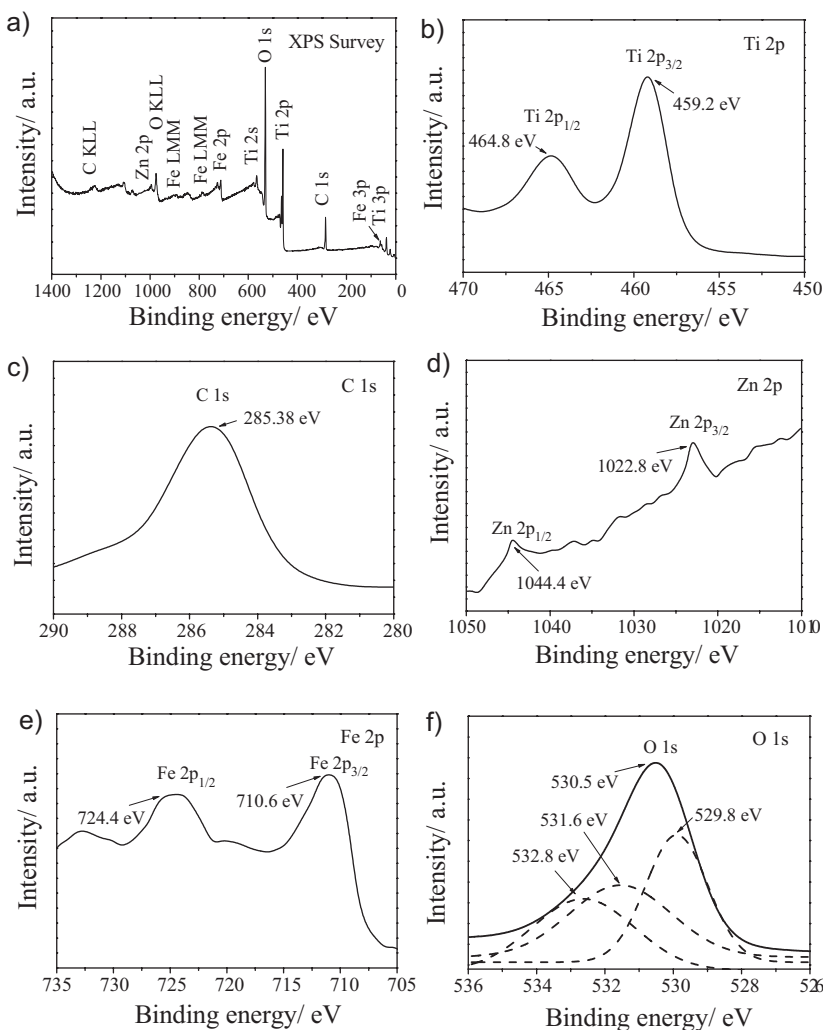


Figure 3. The whole XPS spectra (a), Ti 2p XPS spectra (b), C 1s XPS spectra (c), Zn 2p XPS spectra (d), Fe 2p XPS spectra (e), and O 1s XPS spectra (f) of $\text{ZnFe}_2\text{O}_4/\text{TiO}_2$ composite nanotube arrays.

surface state distribution, and so on. Quick evaluation of the photocatalytic activity could be achieved through proper analysis of the obtained information on the bandgap, surface states, photogenerated charges separation, and transfer behavior.^[68]

Figure 4a presents the SPV spectra of Ti substrate, TiO₂ nanotube arrays, and ZnFe₂O₄/TiO₂ composite nanotube arrays. Ti substrate showed no response to light illumination. In contrast, TiO₂ nanotube arrays exhibited distinguished SPV response. The strong SPV response peak at approximately 360 nm can be attributed to the electron transition from valence band to conduction band of TiO₂ (O_{2p}–Ti_{3d}).^[68] When the TiO₂ nanotube arrays were loaded with ZnFe₂O₄ nanoparticles, the SPV response improved obviously and extended from UV to visible light region, which is in good agreement with the results of DRS. The stronger photovoltage intensity of ZnFe₂O₄/TiO₂ composite nanotube arrays indicates the higher charge separation efficiency as compared with that of TiO₂ in the UV light region. Also, there is additional visible absorption for the ZnFe₂O₄/TiO₂ composite nanotube arrays obviously, which indicates a lower light excitation threshold with respect to the original TiO₂ nanotube arrays. The separation efficiency of electron and hole generated by ZnFe₂O₄ could be also promoted through the connection with TiO₂ nanotubes arrays.

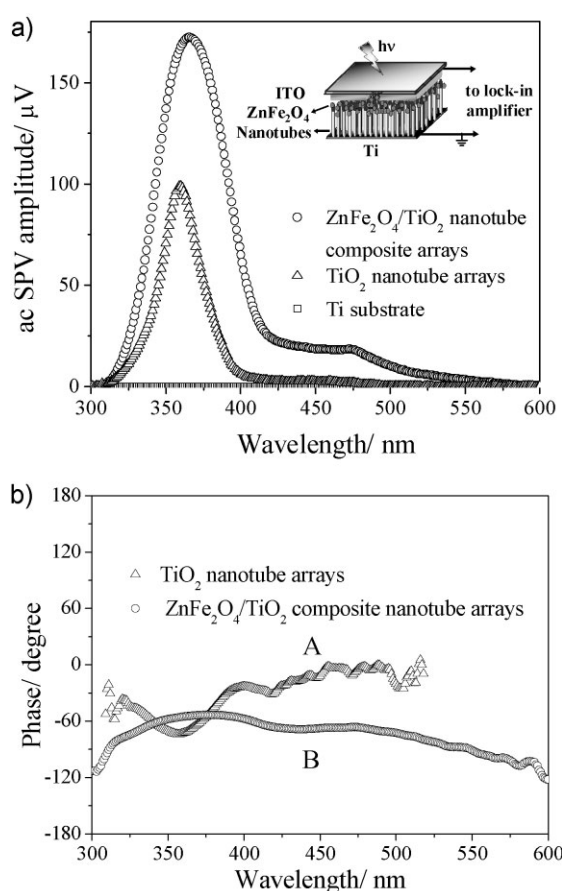


Figure 4. AC SPV spectra (a) and the corresponding phase spectra (b) of Ti substrate, TiO₂ nanotube arrays, and the ZnFe₂O₄/TiO₂ composite nanotube arrays, respectively.

In Figure 4b, the corresponding phase spectra show the statistic kinetic characteristics for each AC SPV spectrum with a distinguishable response. For the two curves, the phase values are under zero, which corresponds to a positive SPV signal.^[69] This sign means that the photogenerated electrons generally transfer towards the Ti substrate electrode from the direction of light incidence. Curve B represents the phase spectrum corresponding to the AC SPV spectrum of ZnFe₂O₄/TiO₂ composite nanotube arrays. The phase retardation relative to 0° with a value of about 70° at 450 nm, which is much larger than TiO₂ nanotube arrays, reflects their discrepant features of photogenerated charge-transfer kinetics. Larger absolute phase retardation means the AC SPV amplitude in one excitation period will take a longer time to reach the balance or saturated value (if possible), statistically. Together with the larger SPV response amplitude for the composite, it is indicated that the photoinduced electron–hole pairs in ZnFe₂O₄/TiO₂ composite nanotube arrays have higher separation efficiency. Hence, an improved photocatalytic activity of the composite nanotube arrays can be expected.

2.2. Current–Voltage Characterization

Figure 5 identifies the current–voltage (*I*–*V*) characteristics of TiO₂ nanotube arrays and ZnFe₂O₄/TiO₂ composite nanotube arrays. The dark current of TiO₂ nanotube arrays is almost zero. However, the *I*–*V* current of the composite arrays shows the difference in the forward and in the reverse direction. The current increased sharply with the positive bias potential and reached nearly 8 μA at 1.2 V, whereas only a low reverse current of 2.2 μA was seen at –1.2 V. The obvious current asymmetry under the forward and reverse bias directions is observed and the rectifying behavior demonstrates the composite have a p–n junction property. This property indicates that a heterojunction might have been established between the TiO₂ nanotubes and ZnFe₂O₄ nanoparticles. The heterojunction could promote separation of photoinduced charge

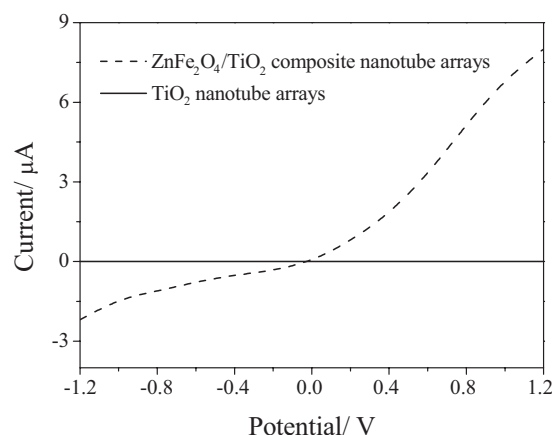


Figure 5. *I*–*V* curve of the TiO₂ nanotube arrays and the ZnFe₂O₄/TiO₂ composite nanotube arrays measured with a micromanipulator manual probe station.

carriers, so that more holes could participate in the redox reactions instead of recombination.

2.3. Photoelectrochemical Measurements

To investigate the influence of the applied potential on the photocurrent magnitude, potentiodynamic scans on the TiO_2 nanotube array electrode and the $\text{ZnFe}_2\text{O}_4/\text{TiO}_2$ composite nanotube array electrode were performed from -0.5 to 1.2 V vs. a saturated calomel electrode (SCE) with a scanning rate of 2 mV s^{-1} under UV light irradiation. Results of the experiment are presented in Figure 6a. As shown, under illumination, a significant

increase in the photocurrent density was observed throughout the potential window at the composite nanotube array electrode. The saturated photocurrent density of the $\text{ZnFe}_2\text{O}_4/\text{TiO}_2$ composite nanotube array electrode (1.62 mA cm^{-2}) was about 1.96 times as high as that of the highly oriented titania nanotubular sample (0.83 mA cm^{-2}) in $0.25 \text{ wt\% NH}_4\text{F}$ and $2.5\% \text{ H}_2\text{O}$ in ethylene glycol solution at 1.2 V (vs. SCE). The dark current densities in all cases could be negligible (Fig. 5).

The photoconversion efficiency η of light energy to chemical energy in the presence of an external applied potential E_{app} , is calculated as^[20]

$$\eta(\%) = \frac{[(\text{total power output} - \text{electrical power input}) / \text{light power input}] \times 100}{j_p [E_{\text{rev}}^\circ - |E_{\text{app}}|] \times 100 / (I_0)} \quad (2)$$

where j_p is the photocurrent density (mA cm^{-2}), $j_p E_{\text{rev}}^\circ$ is the total power output, $j_p |E_{\text{app}}|$ is the electrical power input, and I_0 is the power density of incident light (mW cm^{-2}). E_{rev}° is the standard state-reversible potential (which is 1.23 V (vs. NHE), the potential corresponding to the Gibbs free energy change per photon in the water-splitting reaction at pH 0), and the applied potential is $E_{\text{app}} = E_{\text{meas}} - E_{\text{aoc}}$, where E_{meas} is the electrode potential (vs. SCE) of the working electrode at which photocurrent was measured under illumination and E_{aoc} is the electrode potential (vs. SCE) of the same working electrode under open circuit conditions, under the same illumination, and in the same electrolyte.

Figure 6b shows the total percent photoconversion efficiency ($\eta_{\text{photo}}(\text{total})$) as a function of applied potential (E_{meas} vs. SCE) for the $\text{ZnFe}_2\text{O}_4/\text{TiO}_2$ composite nanotube array electrode and TiO_2 nanotube array electrode under UV light irradiation. A maximum photoconversion efficiency of 28.33% was observed at an applied potential of 0.28 V vs. SCE for the $\text{ZnFe}_2\text{O}_4/\text{TiO}_2$ composite nanotube array electrode, while it was 16.16% for the TiO_2 nanotube array electrode at 0.1 V vs. SCE. In order to utilize more light energy and less electricity energy, the potential of 0.8 V was selected as the proper bias for the $\text{ZnFe}_2\text{O}_4/\text{TiO}_2$ composite nanotube array electrode in photoelectrocatalysis.

Furthermore, the transient photocurrent of TiO_2 nanotube array electrode and $\text{ZnFe}_2\text{O}_4/\text{TiO}_2$ composite nanotube array electrode measured at a fixed bias potential of 0.2 V vs. SCE with a UV light pulse of 50 s is also shown in Figure 6c. The rise and fall of the photocurrent corresponded well to the illumination being switched on and off. The generation of photocurrent consisted of two steps that the first step of the photocurrent appeared promptly after the illumination, and the second step of the photocurrent reached a steady state. This pattern of photocurrent was highly reproducible for numerous on/off cycles of illumination. When the illumination was interrupted, the current rapidly dropped to almost zero. Upon illumination, the photocurrent reverted back to the original steady state value within a couple of seconds ($>90\%$ of the steady state value was obtained instantaneously). In Figure 6c, the short-circuit photocurrent density of $\text{ZnFe}_2\text{O}_4/\text{TiO}_2$ composite nanotube array electrode was more than 0.56 mA cm^{-2} , whereas that of TiO_2 nanotube array electrode was less than 0.35 mA cm^{-2} ; the short-circuit photocurrent of the composite array electrode was more than 1.6 times that of TiO_2 nanotube

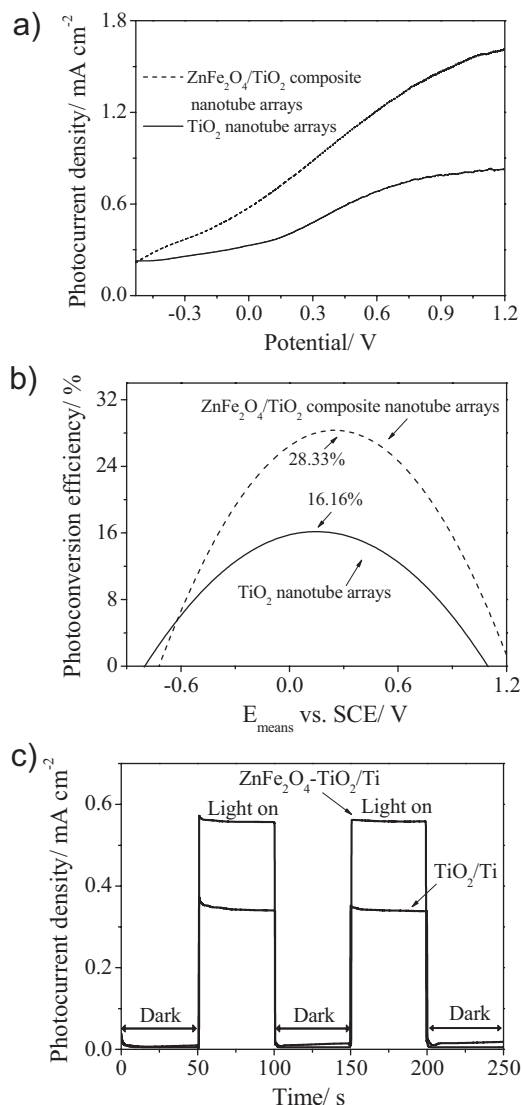


Figure 6. a) Variation of photocurrent density vs. bias potential (vs. SCE). b) Photoconversion efficiency as a function of applied potential (vs. SCE). c) Short-circuit photocurrent density vs. time plotted for TiO_2 nanotube array electrode and $\text{ZnFe}_2\text{O}_4/\text{TiO}_2$ composite nanotube array modified electrode in $0.01 \text{ M Na}_2\text{SO}_4$ solution under UV light irradiation ($I_0 = 2.6 \text{ mW cm}^{-2}$).

array electrode. This result indicated that the separation rate of photogenerated holes and electrons increased due to the formation of a heterojunction, which was in accordance with the SPV measurements. In addition, more photogenerated holes survived from recombination or from the longer lifetime the holes had, which possessed better photoelectrocatalytic activity than did TiO₂ nanotube array electrode.

According to DRS analysis, the absorption edge of ZnFe₂O₄/TiO₂ composite nanotube array electrode successfully extended to the visible light region. Therefore, the photoelectrochemical measurements of TiO₂ nanotube array electrode and the composite nanotube array electrode were carried out to measure the photoresponse of the electrodes under visible light illumination. The variation of the photocurrent density as a function of measured potential vs. SCE have been shown by the representative *I*-*V* characteristics as in Figure 7a. The photocurrents are calculated from the measured currents subtracting the respective dark one, which is negligibly low (Fig. 5). For the two samples, an initial fast increase in the photocurrent was recorded, followed by a gradual stability of the photocurrent with time under visible light illumination. The saturated photocurrent density of the ZnFe₂O₄/TiO₂ composite nanotube array electrode (0.74 mA cm⁻²) was about 3.52 times as high as that of TiO₂ nanotube array (0.21 mA cm⁻²) at 1.2 V (vs. SCE).

Figure 7b shows the corresponding photoconversion efficiency of the two electrodes. A maximum photoconversion efficiency of 0.91% was observed at an applied potential of 0.02 V vs. SCE for the ZnFe₂O₄/TiO₂ composite nanotube array electrode, while it was 0.18% for the TiO₂ nanotube array electrode at 0.3 V vs. SCE. Accordingly, the photoconversion efficiency of the ZnFe₂O₄/TiO₂

composite array electrode could be up to 5.1 times higher than that of the TiO₂ nanotube array electrode, implying that under the same irradiation with the same bias potential, more photoexcited electrons on the heterojunction array electrode flow to the cathode, leaving more photoexcited holes involved in the oxidation reaction.

In addition, the photoresponse test of the composite nanotube arrays was also carried out by potentiostatic (current vs. time, *I*-*t*) measurements under intermittent illumination. Figure 7c shows the *I*-*t* curve obtained from the TiO₂ nanotube array electrode and the ZnFe₂O₄/TiO₂ composite nanotube array electrode with a visible light pulse of 50 s. The photocurrent value goes down to zero as soon as the illumination of light on the photoanode is stopped, and the photocurrent comes back to the original value as soon as light is illuminated again on the electrode. It indicates that the current is completely due to the photoactivity of the catalyst and that the charge-transport is very fast. Clearly, the short-circuit photocurrent density of the composite nanotube array electrode (about 0.49 mA cm⁻²) was approximately 4.9 times as large as that of TiO₂ nanotube array electrode (about 0.1 mA cm⁻²), implying that an electrochemically synthesized ZnFe₂O₄ nanoparticles can be used to sensitize the TiO₂ nanotube array electrode making it more responsive to the visible light spectrum, and thus, may find its application in photoelectrocatalytic degradation of organics under visible light irradiation.

Furthermore, as indicated in Figure 7d, very weak current was observed on the ZnFe₂O₄/TiO₂ composite nanotube array electrode in the dark. While under visible light illumination and no bias potential being applied on the ZnFe₂O₄/TiO₂ composite nanotube array electrode, an average 0.49 mA cm⁻² photocurrent densities was observed. When 0.4, 0.8, and 1.2 V (vs. SCE) were applied to the composite electrode, the photocurrent densities were increased to average 0.56, 0.65, and 0.74 mA cm⁻², respectively. Therefore, the generation of visible-light photocurrent is ascribed to the modification of ZnFe₂O₄ for the TiO₂ nanotube array electrode, which significantly extends the photoresponse from UV to visible light region.

2.4. Photoelectrocatalytic Activities

Figure S4 depicts different processes including electrochemical process (EP), direct photolysis (DP), photocatalysis (PC), and photoelectrocatalysis (PEC) of 4-chlorophenol (4-CP) degradation under UV light irradiation. After 120 min irradiation, the concentration of 4-CP was almost unchanged in the EP, while the 45% of 4-CP was degraded in the DP process without any photocatalyst. The degradation efficiency of 4-CP by PC was 72% with the ZnFe₂O₄/TiO₂ composite nanotube array electrode, whereas it was 66.2% with the unloaded one. When a bias potential of 0.8 V (vs. SCE) was applied, the degradation efficiency increased from 84% for the unloaded TiO₂ nanotube array electrode to 100% for the ZnFe₂O₄-loaded one. From the increased degradation efficiency, there was an

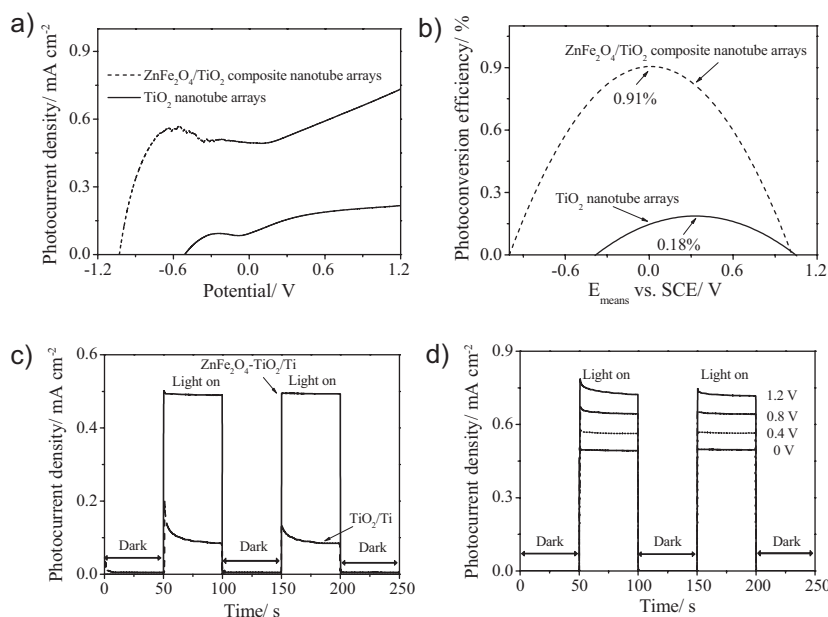
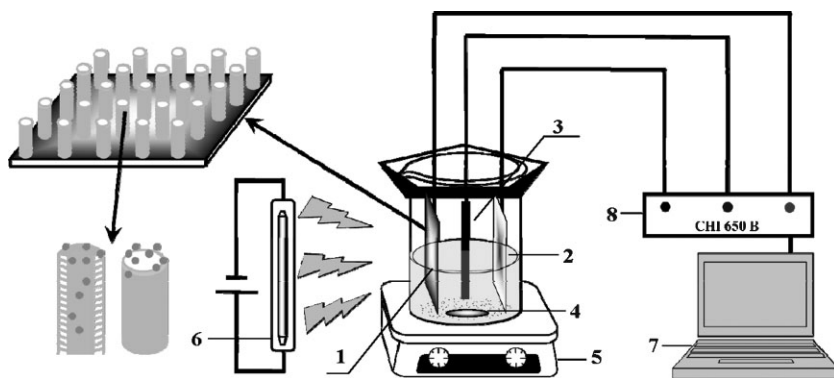


Figure 7. a) Variation of photocurrent density vs. bias potential (vs. SCE). b) Photoconversion efficiency as a function of applied potential (vs. SCE). c) Short-circuit photocurrent density vs. time plotted for TiO₂ nanotube array electrode and ZnFe₂O₄/TiO₂ composite nanotube array modified electrode in 0.01 M Na₂SO₄ solution under visible light irradiation (100 mW cm⁻²). d) Photocurrent densities vs. time of ZnFe₂O₄/TiO₂ composite nanotube array modified electrode being applied with different bias potentials (vs. SCE) under visible light irradiation (100 mW cm⁻²).



Scheme 2. Photoelectrochemical reactor: 1) working electrode ($\text{ZnFe}_2\text{O}_4/\text{TiO}_2$); 2) counter electrode (Pt); 3) reference electrode (SCE); 4) stir bar; 5) magnetic stirrer; 6) high-pressure mercury lamp (Xe lamp); 7) computer; 8) electrochemical workstation.

obvious synergetic effect between the EC process and the PC process, suggesting that the applied bias potential inhibited the recombination of photogenerated electron-hole pairs effectively and prolonged the life of the photogenerated carriers, hence yielding the better performance of PEC. The kinetics of 4-CP degradation in EP, DP, PC, and PEC processes followed pseudo-first-order kinetics, which is described in the Supporting Information, Figure S5. In addition, the $\text{ZnFe}_2\text{O}_4/\text{TiO}_2$ composite nanotube array electrode exhibited remarkable photoelectrocatalytic stability with little loss even after five cycles (Supporting Information, Fig. S6).

3. Conclusions

A $\text{ZnFe}_2\text{O}_4/\text{TiO}_2$ composite nanotube array photoelectrode was successfully prepared by using a novel electrodeposition technique, which effectively promoted deposition of p-type ZnFe_2O_4 nanoparticles within self-organized and vertically oriented n-type TiO_2 nanotubes while minimizing the clogging of the tube entrances. The highly ordered TiO_2 nanotube arrays was self-assembled by the potentiostatic anodization without the use of any templates, which resulted in vertically oriented nanotubular arrays with a tube length of 800–1000 nm. *I*–*V* curves demonstrated that the composite nanotube arrays showed typical heterojunction characteristics. The loading of ZnFe_2O_4 nanoparticles significantly extended the response of the TiO_2 nanotube-array into the visible region and exhibited a higher photovoltage response. The $\text{ZnFe}_2\text{O}_4/\text{TiO}_2$ composite nanotube arrays showed marked photocurrent and improved photoconversion efficiency due to better charge separation and collection efficiency under UV or visible light illumination. Moreover, the composite electrode was found to possess excellent photoelectrocatalytic activity for the degradation of 4-CP under UV light illumination. The composite materials are expected to have promising applications in photocatalysis, solar cells and other light harvesting devices.

4. Experimental

Preparation of the $\text{ZnFe}_2\text{O}_4/\text{TiO}_2$ Composite Nanotube Arrays: Titanium foil (purity 99.6%, thickness 0.25 mm) was obtained from Beijing Academy

of Steel Service, China. All the other chemicals were of analytical grade and were used as received without further purification. Prior to any electrochemical treatment, the titanium foil was first mechanically polished with different abrasive papers, rinsed in an ultrasonic bath of ethanol (20 mL) for 5 min and deionized water (20 mL) for 15 min in turn, and then chemically etched by immersing in a mixture of HF and HNO_3 ($\text{HF}/\text{HNO}_3/\text{H}_2\text{O} = 1:4:5$ in volume, total 20 mL) for 20 s, and finally rinsed in deionized water. The substrate was dried in a N_2 stream at room temperature (approximately 22 °C). The anodization was performed with use of a two-electrode cell with titanium foil as the working electrode and platinum foil as the counter electrode at room temperature. The anodizing voltage varied from 0 to 20 V with an increasing rate of 100 mV s^{-1} and was kept at 20 V for 1 h. The electrolytes were 0.25 wt% NH_4F (0.28 g, 7.56 mmol) and 2.5% H_2O (2.5 mL) in ethylene glycol (97.5 mL). The pH of the electrolyte was adjusted to 6 by the solution of 2 M H_2SO_4 . The anodization current

was monitored using a power management system (array electronic 3646A) interfaced with a computer. After anodization, the sample was immediately rinsed with deionized water and dried with a N_2 stream. Then it was annealed at 773 K in air for 1 h with heating and cooling rates of 2 °C min^{-1} to convert the amorphous phase to the crystalline one. A conventional three-electrode setup in an undivided cell was used for cathodic deposition, using the system with a TiO_2 nanotube array electrode as the working electrode, a Pt foil as the counter electrode, and a SCE as the reference electrode. The potentiostatic DC electrodeposition was carried out with a potential of -0.8 V for 20 min and the temperature of the electrolyte was maintained at 85 °C. Before electrodeposition, this sample is then soaked in a mixture solution (100 mL) containing 0.05 M (1.48 g) zinc nitrate heptahydrate ($\text{Zn}(\text{NO}_3)_2 \cdot 6\text{H}_2\text{O}$) and 0.1 M (4.04 g) ferric nitrate nonahydrate ($\text{Fe}(\text{NO}_3)_3 \cdot 9\text{H}_2\text{O}$) for 20 min under ultrasonication. The ultrasonication processes help the salt solution to diffuse through the nanochannels of TiO_2 and ensure that the inner wall of the pore channel was wetted. Then the TiO_2 nanotube array electrode is transferred into a new medium that contains only an inert supporting electrolyte (0.1 M Na_2SO_4 , 100 mL) without Zn^{2+} and Fe^{3+} . The deposition after immersion in this medium results in deposition of Zn and Fe only within the pores while minimizing deposition at the tube entrances. A desired deposition amount of Zn and Fe in the pores was obtained after ultrasonication and deposition procedure 10 repetitions (the concentration of the $\text{Zn}(\text{NO}_3)_2 \cdot 6\text{H}_2\text{O}$ and $\text{Fe}(\text{NO}_3)_3 \cdot 9\text{H}_2\text{O}$, dipping time, deposition potential, and number of cycles were decided by the detailed experimental analysis in the Supporting Information). After electrodeposition, the as-electrodeposited material was electrochemically oxidized at room temperature using another alkaline electrolytic bath prepared by dissolving 1 M KOH (100 mL) in distilled water. This time the electrode with the electrodeposited material was connected as the anode and Pt foil as the cathode. The separation between them was 1 cm and a constant potential of 1.6 V was applied for 2 min. After electrochemical oxidization, the samples were thoroughly rinsed with acetone, methanol, and deionized water. The annealed samples were prepared by heating at 773 K for 120 min, with a ramp of 2 °C min^{-1} (Scheme 1).

Characterization Methods: The morphology of the $\text{ZnFe}_2\text{O}_4/\text{TiO}_2$ composite nanotube arrays were characterized using an ESEM (Quanta 200 FEG) with an accelerating voltage of 30.0 kV. The dopant concentration was verified by EDX (Horiba 7593H), and EDX was performed to determine the elemental concentration distribution on the catalyst granules using Link Isis Series 300 software. A small amount of sample was placed in a carbon-coated grid and subjected for HRTEM measurements. The crystallinity of the prepared samples was determined from XRD using a diffractometer with $\text{Cu K}\alpha$ radiation (Shimadzu Lab-X XRD-6000, source light at the wavelength (λ) of 0.15406 nm). The accelerating voltage and applied current were 40 kV and 30 mA, respectively. The diffraction angles (2θ) were scanned from 20° to 60° with a scan rate of 10° min^{-1} and step distance of

0.02°. The average crystallite sizes were determined according to the Scherrer equation using the full-width half-maximum data after correcting the instrumental broadening. High-grade silicon powder was used as a standard to allow for the instrument broadening correction. Individual peaks were fitted using the Siemens Diffrac-AT software package to extract experimental full widths at half-maximum and integral widths. In addition, the micro-strain broadening profile coefficients were also converted according to the reported procedure [70]. Light absorption properties were measured using UV-Vis DRS (JASCO, UV-550) with a wavelength range of 200–800 nm. FL analyses were measured at room temperature using an RPM2000 spectrophotometer (ACCENT Semiconductor Technologies Ltd., UK) with a He-Cd laser ($\lambda = 325$ nm) as the light source. XPS (PHI 5600 mode) was performed to examine the surface properties and composition of the sample. All the binding energies were calibrated by using the contaminant carbon (C 1s) 284.6 eV as a reference. The separation characteristics of photogenerated charge carriers were tested by a lock-in-based SPV measurement system, which consists of a monochromator (model Omni- λ 3005) and a lock-in amplifier (model SR830-DSP) with an optical chopper (model SR540) running at a frequency of 20 Hz. All of the SPV measurements were performed at room temperature.

Photoelectrochemical Measurements: Photocurrent density was measured using a CHI electrochemical analyzer (CH instruments 650B, Shanghai Chenhua, China) in a standard three-electrode configuration with the ZnFe₂O₄/TiO₂ composite nanotube arrays as photoanode (an effective area of 6 cm²), a platinum foil as counter electrode, and a SCE as reference electrode. 0.01 M Na₂SO₄ (100 mL) purged with N₂ was used as the electrolyte. A 300 W high-pressure mercury lamp (Southern New England Ultraviolet Lighting Co.) served as the UV-light source with a principal wavelength of 365 nm ($I_0 = 2.6$ mW cm⁻²). In addition, a 500 W high-pressure xenon short arc lamp (Phillips) with a filter to remove light of wavelength below 400 nm was used as the visible light source to provide a light intensity of 100 mW cm⁻² (Scheme 2).

Photoelectrocatalytic Experiment: The PEC degradation of 4-CP was performed in a single photoelectrochemical compartment. The ZnFe₂O₄/TiO₂ composite nanotube array photoanode was in parallel with platinum foil cathode in a cylindrical quartz reactor with magnetic stirring, and a SCE served as the reference electrode. The electrodes were connected to a DJ5-292 potentiostat (France Radiometer Limited). The high-pressure mercury lamp was placed vertically outside the reactor (Supporting Information, Scheme S1). Bias potentials applied on photoanode were 0.8 V (vs. SCE) under UV light illumination (with a maximum wavelength of 365 nm, $I_0 = 2.6$ mW cm⁻²). The initial concentration of 4-CP aqueous solution was 20 mg L⁻¹ with 0.01 M Na₂SO₄ as electrolyte (pH 7.0).

Acknowledgements

This work was supported financially by the National Nature Science Foundation of China (No.20877013, No.20837001), the National High Technology Research and Development Program of China (863 Program) (No. 2007AA061402), the Major State Basic Research Development Program of China (973 Program) (No. 2007CB613306), the Fok Ying Tung Foundation (NRC07/08.EG01), and the Changjiang Scholars and Innovative Research Team in University. Supporting Information is available online from Wiley InterScience or from the author.

Received: December 18, 2009

Revised: March 29, 2010

Published online: May 25, 2010

[1] X. Chen, S. S. Mao, *Chem. Rev.* **2007**, *107*, 2891.

[2] J. Nowotny, T. Bak, M. K. Nowotny, L. R. Sheppard, *J. Phys. Chem. B* **2006**, *110*, 18492.

[3] J. Zhang, Q. Xu, Z. C. Feng, M. J. Li, C. Li, *Angew. Chem. Int. Ed.* **2008**, *47*, 1766.

[4] B. O. Regan, M. Grätzel, *Nature* **1991**, *353*, 737.

- [5] G. K. Mor, K. Shankar, M. Paulose, O. K. Varghese, C. A. Grimes, *Nano Lett.* **2006**, *6*, 215.
- [6] K. W. Park, Y. E. Sung, *Inorg. Chem.* **2005**, *44*, 3190.
- [7] G. F. Ortiz, I. Hanzu, T. Djenizian, P. Lavela, J. L. Tirado, P. Knauth, *Chem. Mater.* **2009**, *21*, 63.
- [8] K. X. Wang, M. D. Wei, M. A. Morris, H. S. Zhou, J. D. Holmes, *Adv. Mater.* **2007**, *19*, 3016.
- [9] J. M. Macak, P. J. Barczuk, H. Tsuchiya, M. Z. Nowakowska, A. Ghicov, M. Chojak, S. Bauer, S. Virtanen, P. J. Kulesza, P. Schmuki, *Electrochem. Commun.* **2005**, *7*, 1417.
- [10] S. P. Albu, A. Ghicov, J. M. Macak, R. Hahn, P. Schmuki, *Nano Lett.* **2007**, *7*, 1286.
- [11] D. Gong, C. A. Grimes, O. K. Varghese, W. Hu, R. S. Singh, Z. Chen, E. C. Dickey, *J. Mater. Res.* **2001**, *16*, 3331.
- [12] M. Law, L. E. Greene, J. C. Johnson, R. Saykally, P. D. Yang, *Nat. Mater.* **2005**, *4*, 455.
- [13] A. J. Frank, N. Kopidakis, J. van de Lagemaat, *Coord. Chem. Rev.* **2004**, *248*, 1165.
- [14] K. Zhu, N. R. Neale, A. Miedaner, A. J. Frank, *Nano Lett.* **2007**, *7*, 69.
- [15] Z. Y. Liu, X. T. Zhang, S. Nishimoto, T. Murakami, A. Fujishima, *Environ. Sci. Technol.* **2008**, *42*, 8547.
- [16] H. F. Zhuang, C. H. Lin, Y. K. Lai, L. Sun, J. Li, *Environ. Sci. Technol.* **2007**, *4*, 4735.
- [17] J. G. Yu, Q. J. Xiang, M. H. Zhou, *Appl. Catal. B* **2009**, *90*, 595.
- [18] H. Y. Chuang, D. H. Chen, *Nanotechnology* **2009**, *20*, 105704.
- [19] S. K. Mohapatra, N. Kondamudi, S. Banerjee, M. Misra, *Langmuir* **2008**, *24*, 11276.
- [20] S. U. M. Khan, M. Al-Shahry, W. B. Ingler, Jr, *Science* **2002**, *297*, 2243.
- [21] M. Bellardita, M. Addamo, A. D. Paola, L. Palmisano, A. M. Venezia, *Phys. Chem. Chem. Phys.* **2009**, *11*, 4084.
- [22] A. Zaleska, E. Grabowska, J. W. Sobczak, M. Gazda, J. Hupka, *Appl. Catal. B* **2009**, *89*, 469.
- [23] M. Batzill, E. H. Morales, U. Diebold, *Phys. Rev. Lett.* **2006**, *96*, 026103.
- [24] D. H. Kim, J. S. Yang, Y. S. Kim, D. W. Kim, T. W. Noh, *Appl. Phys. Lett.* **2003**, *83*, 4574.
- [25] J. W. Tang, Z. G. Zou, J. H. Ye, *Angew. Chem. Int. Ed.* **2004**, *43*, 4463.
- [26] K. Maeda, K. Teramura, D. Lu, T. Takata, N. Saito, Y. Inoue, K. Domen, *Nature* **2006**, *440*, 295.
- [27] D. F. Wang, T. Kako, J. H. Ye, *J. Am. Chem. Soc.* **2008**, *130*, 2724.
- [28] D. Berthebaud, F. Grasset, V. Allegret-Maret, S. Ababou-Girard, S. Pechev, *J. Phys. Chem. C* **2007**, *111*, 7883.
- [29] F. Grasset, G. Starukh, L. Spanhel, S. Ababou-Girard, D. S. Su, A. Klein, *Adv. Mater.* **2005**, *17*, 294.
- [30] D. R. Baker, P. V. Kamat, *Adv. Funct. Mater.* **2009**, *19*, 805.
- [31] S. Banerjee, S. K. Mohapatra, P. P. Das, M. Misra, *Chem. Mater.* **2008**, *20*, 6784.
- [32] M. Shalom, S. Rühle, I. Hod, S. Yahav, A. Zaban, *J. Am. Chem. Soc.* **2009**, *131*, 9876.
- [33] C. Ratanatawanate, Y. Tao, K. J. Balkus, Jr, *J. Phys. Chem. C* **2009**, *113*, 10755.
- [34] C. Ratanatawanate, C. Xiong, K. J. Balkus, Jr, *ACS Nano* **2008**, *2*, 1682.
- [35] R. Brahimi, Y. Bessekhouad, A. Bouguelia, M. Trari, *Catal. Today* **2007**, *122*, 62.
- [36] L. M. Peter, K. G. U. Wijayantha, D. J. Riley, J. P. Waggett, *J. Phys. Chem. B* **2003**, *107*, 8378.
- [37] Y. L. Lee, B. M. Huang, H. T. Chien, *Chem. Mater.* **2008**, *20*, 6903.
- [38] S. Q. Fan, D. Kim, J. J. Kim, D. W. Jung, S. O. Kang, J. Ko, *Electrochem. Commun.* **2009**, *11*, 1337.
- [39] N. Guijarro, T. Lana-Villarreal, I. Mora-Seró, J. Bisquert, R. Gómez, *J. Phys. Chem. C* **2009**, *113*, 4208.
- [40] G. Y. Lan, Z. Yang, Y. W. Lin, Z. H. Lin, H. Y. Liao, H. T. Chang, *J. Mater. Chem.* **2009**, *19*, 2349.
- [41] J. H. Bang, P. V. Kamat, *ACS Nano* **2009**, *3*, 1467.
- [42] X. F. Gao, H. B. Li, W. T. Sun, Q. Chen, F. Q. Tang, L. M. Peng, *J. Phys. Chem. C* **2009**, *113*, 7531.

- [43] F. Grasset, N. Labhsetwar, D. Li, D. C. Park, N. Saito, H. Haneda, O. Cador, T. Roisnel, S. Mornet, E. Duguet, J. Portier, J. Etourneau, *Langmuir* **2002**, *18*, 8209.
- [44] F. F. Liu, X. Y. Li, Q. D. Zhao, Y. Hou, X. Quan, G. H. Chen, *Acta Mater.* **2009**, *57*, 2684.
- [45] M. K. Roy, H. C. Verma, *J. Magn. Magn. Mater.* **2006**, *306*, 98.
- [46] F. S. Li, H. B. Wang, L. Wang, J. B. Wang, *J. Magn. Magn. Mater.* **2007**, *309*, 295.
- [47] N. Ponpandian, A. Narayanasamy, *J. Appl. Phys.* **2002**, *92*, 2770.
- [48] R. Zhang, J. Huang, J. Zhao, Z. Sun, Y. Wang, *Energy Fuels* **2007**, *21*, 2682.
- [49] M. Kobayashi, H. Shirai, M. Nunokawa, *Energy Fuels* **2002**, *16*, 1378.
- [50] J. Philip, G. Gnanaprakash, G. Panneerselvam, M. P. Antony, T. Jayakumar, B. Raj, *J. Appl. Phys.* **2007**, *102*, 054305.
- [51] C. J. He, B. S. Zou, Z. Y. Wu, Y. X. Nie, *Opt. Commun.* **2008**, *281*, 851.
- [52] Y. Zeng, J. T. Liu, W. Wu, C. X. Ding, *Surf. Coat. Technol.* **2005**, *200*, 2398.
- [53] J. Yin, L. J. Bie, Z. H. Yuan, *Mater. Res. Bull.* **2007**, *42*, 1402.
- [54] S. H. Xu, D. L. Feng, W. F. Shangguan, *J. Phys. Chem. C* **2009**, *113*, 2463.
- [55] S. K. Mohapatra, S. Banerjee, M. Misra, *Nanotechnology* **2008**, *19*, 315601.
- [56] H. E. Prakasam, K. Shankar, M. Paulose, O. K. Varghese, C. A. Grimes, *J. Phys. Chem. C* **2007**, *111*, 7235.
- [57] S. K. Mohapatra, M. Misra, V. K. Mahajan, K. S. Raja, *J. Phys. Chem. C* **2007**, *111*, 8677.
- [58] P. Roy, D. Kim, K. Lee, E. Spiecker, P. Schmuki, *Nanoscale* **2010**, *2*, 45.
- [59] A. Ghicov, P. Schmuki, *Chem. Commun.* **2009**, 2791.
- [60] G. K. Mor, O. K. Varghese, M. Paulose, K. Shankar, C. A. Grimes, *Sol. Energy Mater. Sol. Cells* **2006**, *90*, 2011.
- [61] P. K. Harold, E. A. Leroy, *X-ray Diffraction Procedures: For Polycrystalline and Amorphous Materials*, Wiley, New York **1974**, p. 618.
- [62] D. G. Lamas, R. O. Fuentes, I. O. Fábregas, M. E. Fernández, G. E. Lascalea, J. R. Casanova, N. E. Walsöe, A. F. Craievich, *J. Appl. Crystallogr.* **2005**, *38*, 867.
- [63] L. H. Huang, C. Sun, Y. L. Liu, *Appl. Surf. Sci.* **2007**, *253*, 7029.
- [64] S. K. Joung, T. Amemiya, M. Murabayashi, K. Itoh, *Chem.-Eur. J.* **2006**, *12*, 5526.
- [65] Y. N. NuLi, Y. Q. Chu, Q. Z. Qin, *J. Electrochem. Soc.* **2004**, *151*, A1077.
- [66] L. Xue, C. B. Zhang, H. He, Y. Teraok, *Appl. Catal. B* **2007**, *75*, 167.
- [67] L. Kronik, Y. Sapira, *Surf. Sci. Rep.* **1999**, *37*, 1.
- [68] L. Q. Jing, X. J. Sun, J. Shang, W. M. Cai, Z. L. Xu, Y. G. Du, H. G. Fu, *Sol. Energy Mater. Sol. Cells* **2003**, *79*, 133.
- [69] V. Donchev, K. Kirilov, Ts. Ivanov, K. Germanova, *Mater. Sci. Eng. B* **2006**, *129*, 186.
- [70] D. Balzar, N. Auderbrand, M. R. Daymond, A. Fitch, A. Hewat, J. I. Langford, *J. Appl. Crystallogr.* **2004**, *37*, 911.